

HyperTea: A Hypergraph-based Temporal Enhancement and Alignment Network for Moving Infrared Small Target Detection

Zhaoyuan Qi¹, Weihua Gao¹, Wenlong Niu¹, Jie Tang¹, Yun Li¹, Xiaodong Peng¹

Abstract—In practical application scenarios, moving infrared small target detection (MIRSTD) remains highly challenging due to the target’s small size, weak intensity, and complex motion pattern. Existing methods typically only model low-order correlations between feature nodes and perform feature extraction and enhancement within a single temporal scale. Although hypergraphs have been widely used for high-order correlation learning, they have received limited attention in MIRSTD. To explore the potential of hypergraphs and enhance multi-timescale feature representation, we propose HyperTea, which integrates global and local temporal perspectives to effectively model high-order spatiotemporal correlations of features. HyperTea consists of three modules: the global temporal enhancement module (GTEM) realizes global temporal context enhancement through semantic aggregation and propagation; the local temporal enhancement module (LTEM) is designed to capture local motion patterns between adjacent frames and then enhance local temporal context; additionally, we further develop a temporal alignment module (TAM) to address potential cross-scale feature misalignment. To our best knowledge, HyperTea is the first work to integrate convolutional neural networks (CNNs), recurrent neural networks (RNNs), and hypergraph neural networks (HGNNs) for MIRSTD, significantly improving detection performance. Experiments on DAUB and IRDST demonstrate its state-of-the-art (SOTA) performance. Our source codes are available at <https://github.com/Lurenjia-LRJ/HyperTea>.

Index Terms—Moving infrared small target detection (MIRSTD), hypergraph learning, temporal context enhancement, hypergraph-based temporal enhancement and alignment Network (HyperTea).

I. INTRODUCTION

Infrared small target detection (IRSTD) has been widely applied in fields such as reconnaissance, surveillance, and rescue [1]. In many practical scenarios, unmanned aerial vehicles (UAVs) represent the primary detection targets. However, the inherent characteristics of infrared imaging systems impose the following challenges on infrared small target detection:

- **Dim-small:** The long imaging distance causes a small target scale, weak intensity, low contrast and low signal-to-clutter ratio (SCR), making targets easily obscured in complex backgrounds.

Manuscript received ; revised . (Corresponding author: Wenlong Niu, Xiaodong Peng.)

Zhaoyuan Qi is with the Key Laboratory of Electronics and Information Technology for Space Systems, National Space Science Center, Chinese Academy of Sciences, Beijing 100190, China, and also with the School of Computer Science and Technology, University of Chinese Academy of Sciences, Beijing 100049, China (e-mail: qizhaoyuan24@mailsucas.ac.cn). Weihua Gao, Wenlong Niu, Jie Tang, Yun Li, and Xiaodong Peng are with the Key Laboratory of Electronics and Information Technology for Space Systems, National Space Science Center, Chinese Academy of Sciences, Beijing 100190, China (e-mail: gaoweihua22@mailsucas.ac.cn, niuwenlong@nssc.ac.cn; tangjie@nssc.ac.cn; liyun02@nssc.ac.cn; Pxd@nssc.ac.cn)

- **Poor Spatial distinguishability:** Owing to the inherent characteristics of infrared imaging systems, targets suffer from the absence of color and texture features and exhibit blurred edges. These factors significantly degrade the spatial distinguishability of targets from clutters.
- **Spatiotemporal instability:** For moving infrared small targets, driven by factors such as distance changes, pose adjustments, or partial occlusions by clutters, their spatial characteristics (e.g., size and intensity) may exhibit dynamic variations across consecutive frames. Concurrently, their motion features (e.g., velocity and trajectory) are influenced by two primary factors: one is the intrinsic motion of targets; the other is imaging platform’s motion and perspective transformations. These two factors collectively induce non-uniform and non-linear motion patterns of targets, thereby posing significant challenges to feature representation learning.
- **Target-Clutter Spatiotemporal Coupling:** Background clutters often bears striking similarities to targets in two critical dimensions. Spatially, their features within single frames are very similar to those of targets. Temporally, their motion patterns may exhibit short-term similarity to targets’, particularly when the imaging platform undergoes changes in position and orientation, where the relative motion of both targets and clutters with respect to the imaging platform becomes highly analogous. This dual similarity encompassing spatial characteristics in single frame and motion trends across consecutive frames induces strong spatiotemporal coupling between clutters and real targets. Such coupling obscures the discriminative cues between the two, thereby significantly increases the difficulty of accurate detection.

To cope with these challenges, many IRSTD methods have been proposed, typically categorized into model-based methods and learning-based methods. Model-based methods leverage prior knowledge derived from image observation and analysis to detect targets [2], [3], [4]. While they perform well in certain scenarios [5], [6], their heavy reliance on manually designed feature extractor and hyperparameter tuning limits their adaptability.

In contrast, learning-based methods have recently shown superior detection performance and generalization ability [7], [8], [9]. These methods primarily rely on CNNs [10], [11], Transformers [12], [13], [14], RNNs [15], and their hybrids. CNN-based methods [8], [16], [17] can effectively extract local features but are constrained by grid-based representations, limiting their ability to model spatial global dependencies. Since transformers overcome this limitation by modeling images as

fully connected graphs, some methods use them to improve long-range modeling [18], [19], [20]. However, the quadratic computational complexity and the lost of low-level details caused by patch embedding may limit their application. RNN-based methods have gained increasing attention due to their excellent ability in modeling sequential dependencies [9], [21]. Nonetheless, they suffer from difficulties in parallel training and high computational costs, especially for long sequences. Recently, as an innovative fundamental network architecture, Hypergraph Neural Networks (HGNNs) present huge potential in general target detection owing to their higher-order learning ability [22], [23], but their application in IRSTD remains to be explored.

Given that each network architecture has inherent limitations and advantages, and existing methods struggle to model semantic associations across different temporal scales, we naturally conceive the idea of exploring a new paradigm for MIRSTD by leveraging complementary advantages of networks and thus achieve multi-timescale learning.

Therefore, a key problem is how to build a detection pipeline based on fundamental network architectures. Inspired by [23], [18], our framework mainly employs RNN to enhance short-term temporal dependencies for its excellent ability of modeling sequential dependencies, and CNN to enhance long-range spatiotemporal contextual relationships for it can extract features efficiently. HGNNs are integrated to endow local and global features with higher-order dependency representation capabilities. And the core components of transformer, attention mechanism, is employed to achieve cross-temporal feature alignment.

To fully leverage the complementary advantages of various basic network architectures and promote cross-temporal feature representation learning of targets, we propose a hypergraph-based temporal enhancement and alignment network (HyperTea). Specifically, our work focuses on representing infrared targets simultaneously at both global and local temporal scales, especially using hypergraphs to enable the learning of high-order correlations. Our HyperTea is not a simple fusion of basic network structures. Instead, it captures high-order correlations, then enhances global and local temporal contexts respectively, and also involves cross-scale alignment. To our best knowledge, this is the first work to integrate CNNs, RNNs, and HGNNs for MIRSTD. In summary, the main contributions of our work are summarized as follows.

- 1) We explore and propose a pioneering three-architecture scheme HyperTea to explore the multi-timescale feature representation learning of MIRSTD, which first integrates CNNs, RNNs, and HGNNs into a unified framework.
- 2) With HGNNs being applied to IRSTD for the first time, we propose two modules to enhance global and local temporal context respectively. Specifically, based on CNN and HGNN, a global temporal enhancement module (GTEM) is developed to extract high-order semantic correlations from the global temporal context and propagate them to each frame for enhancement. Additionally, we improve ConvLSTM by HGNN and

thus design the local temporal enhancement module (LTEM) to enhance local inter-frame correlations of small targets.

- 3) A temporal alignment module (TAM) is designed to diminish the potential misalignment between features across different temporal scales, and amplify the semantic differences between target and background.

II. RELATED WORK

A. Hypergraph Learning

As shown in [24], [22], hypergraphs exhibit impressive capabilities in modeling complex higher-order associations and have been applied in various fields [25], [26], [27]. Recently, general hypergraph neural network [22] introduces a spatial approach for higher-order message propagation among feature vertices and achieves remarkable detection performance. Despite these advancements, the application of hypergraph learning remains to be explored in IRSTD.

B. Infrared Small Target Detection

According to different driven paradigms, IRSTD methods can be categorized into model-based methods and learning-based methods. Model-based methods can be further divided into filter-based methods [28], [3], local contrast-based methods [2], [29], [30], [31], and low-rank representation-based methods [4], [5]. These methods usually rely on specific hypotheses, manually designed feature extractors, and hyperparameters based on prior knowledge. Such dependencies often limit their generalization ability in complex real-world scenarios [9]. In contrast, learning-based methods achieve superior detection performance due to their powerful feature representation and learning ability. Depending on the number of reference frames used, learning-based methods can be further classified into single-frame and multi-frame schemes.

As a prominent research direction, single-frame schemes have recently attracted significant attention. CNN-based methods are typically built upon U-Net [32] and its variants, with feature fusion serving as a representative improvement strategy. For example, ACM [7] realizes feature fusion of different levels through asymmetric context modulation. DNANet [8] achieves better detection performance through gradual interaction and enhancement between high-level and low-level features. To reach multilevel and multiscale representation learning, UTUNet [16] embeds a tiny U-Net into a larger U-Net backbone. ISNet [33] extracts the underlying edge features and improves detection performance through cross-layer feature fusion. RDIAN [34] utilizes multiscale convolution and direction-induced attention mechanisms to capture richer target features for fusion. Recently, many studies have combined CNNs with ViTs [13] to leverage their significant advantage in modeling long-range dependencies. IR-TransDet [20] explores the relationship between the global image, the target, and the neighboring pixels. SCTransNet [18] efficiently encodes semantic differences between target and background via spatial channel cross-transformers. Inspired by the ODE, RKformer [35] and ABMNet [36] are proposed. Considering the high labeling costs of full supervision, point-supervision

schemes [37], [38], [39], [40], [41], [42] and self-supervision schemes [43] have emerged as viable alternatives. Recently, some popular network architectures such as Mamba [44], SAM [45] are also migrated to IRSTD. However, the lack of motion information limits single-frame schemes in detecting moving infrared targets under complex dynamic backgrounds. To overcome this problem, some multi-frame strategies have been proposed recently.

Depending on the primary network architecture, multi-frame schemes can be further categorized into CNN-based, CNN with transformer, and CNN with RNN approaches. CNN-based schemes such as STDManet [46], which proposes spatiotemporal differential multiscale attention networks. DTUM [47] uses direction-coded convolution to extract target motion features. TMP [48] extracts temporal and spatial features in parallel and performing cross-domain feature fusion. As for CNN with transformer methods, ST-Trans [19] models spatiotemporal correlations through improved Video Swin Transformer [14]. Tridos [49] uses Video Swin Transformer [14] to capture global frequency-domain features. To exploit the powerful temporal modeling ability of RNNs, CNN with RNN schemes like SSTNet [9] models spatiotemporal features in cross-slice motion context based on improved ConvLSTM [15]. Furthermore, in terms of weakly supervised learning, S2MVP [50] achieves remarkable performance using a small number of labeled training samples. In order to utilize prior knowledge in linguistic cues, visual-language detection frameworks MoPKL [51] are gradually attracting the attention.

However, current IRSTD methods has not yet involved cross-temporal scales (local-global time range) context modeling. Additionally, existing methods can only capture low-order correlations between feature nodes and fail to model correlations among multiple nodes. How to model high-order correlations between nodes and utilize them to enhance motion context remains to be explored.

In view of this, we focus on target feature enhancement and alignment across temporal scales, particularly using HGNNs to learn high-order correlations. For intuitiveness and clarity, we summarize the unique advantages of our HyperTea as follows:

- 1) To overcome the limitation of learning-based multi-frame methods that capture infrared target features at a single temporal scale, we consider enhancing target features at both local and global temporal scales.
- 2) Traditional networks such as CNNs and Transformers can only model low-order relationships between nodes. Considering the complex many-to-many relationships among nodes, we introduce HGNNs into IRSTD.
- 3) Traditional learning-based methods fail to leverage the complementary advantages among basic network structures. Given this, we design a new HyperTea to address it.

III. METHODOLOGY

A. Preliminaries

Compared to ordinary graphs, the most important feature of hypergraphs is that hyperedges can be associated with multiple

vertices, thus makes it possible to model more complex higher-order relationships. A hypergraph [22] can be defined as $\mathcal{G} = \{\mathcal{V}, \mathcal{E}\}$, where \mathcal{V} is the vertex set and \mathcal{E} is the hyperedge set. Typically, a distance-based approach is used to construct \mathcal{E} . Based on the spatial-domain hypergraph convolution with extra residual connections [23], a hypergraph convolution unit (HCU) can be formulated as:

$$\begin{aligned} \text{HCU}(\mathbf{X}) &= \text{HyperConv}(\mathbf{X}, \mathbf{H}) \\ &= \mathbf{X} + \mathbf{D}_v^{-1} \mathbf{H} \mathbf{D}_e^{-1} \mathbf{H}^T \mathbf{X} \Theta \end{aligned} \quad (1)$$

where \mathbf{H} represents the incidence matrix of \mathbf{X} , \mathbf{D}_v and \mathbf{D}_e represent the diagonal degree matrices of the vertices and hyperedges respectively, Θ is a fully connected layer.

Hypergraph convolution can be understood as follows. The multiplication of \mathbf{H}^T facilitates the information aggregation from nodes to hyperedges, followed by normalization using \mathbf{D}_e . Subsequently, multiplying with \mathbf{H} aggregates information from hyperedges back to vertices, with normalization performed via \mathbf{D}_v . Through this two-stage information propagation, hypergraph convolution can model the high-order correlations between vertices.

B. Overall Architecture

We aim to effectively improve the network's ability of detecting moving small targets through cross-temporal feature learning. To achieve this goal, we propose a new framework, as shown in Figure 1. For clarity, its simplified workflow is presented in Figure 2.

Our HyperTea starts with T consecutive frames $\mathbf{I}_s = [\mathbf{I}_1, \mathbf{I}_2, \dots, \mathbf{I}_T]$ as input and outputs the detection results on keyframe \mathbf{I}_T . Following the common paradigm of MIRSTD [9], [48], [49], we use the Cross-Stage Partial Darknet (CSPDarknet) [52] as the backbone. To realize the strategy of cross-temporal feature learning, we design three key modules: GTEM, LTEM, and TAM.

As for the pipeline, we first feed each frame into the backbone with shared weights to obtain multi-frame spatial features $\mathbf{F}_s = \{\mathbf{F}_1, \mathbf{F}_2, \dots, \mathbf{F}_T\} \in \mathbb{R}^{T \times C \times H \times W}$, where C , H , and W denote the channel, height and width of feature, respectively. After that, GTEM receives \mathbf{F}_s as its input and output the global temporal context-enhanced feature $\mathbf{G}_{st} = \{\mathbf{G}_1, \mathbf{G}_2, \dots, \mathbf{G}_T\} \in \mathbb{R}^{T \times C \times H \times W}$. LTEM also receives \mathbf{F}_s as its input and output the local temporal context-enhanced feature $\mathbf{L}_{st} \in \mathbb{R}^{C \times H \times W}$. To achieve the aggregation of global and local temporal context, we then feed \mathbf{G}_{st} and \mathbf{L}_{st} into TAM to mitigate misalignment at different temporal scales. The above pipeline can be formulated as follows:

$$\begin{cases} \mathbf{G}_{st} &= \text{GTEM}(\mathbf{F}_s) \\ \mathbf{L}_{st} &= \text{LTEM}(\mathbf{F}_s) \\ \mathbf{F}_{gl} &= \text{TAM}(\mathbf{G}_{st}, \mathbf{L}_{st}) \end{cases} \quad (2)$$

Finally, the global-local aligned temporal feature \mathbf{F}_{gl} is fed into the detection head to obtain the detection results.

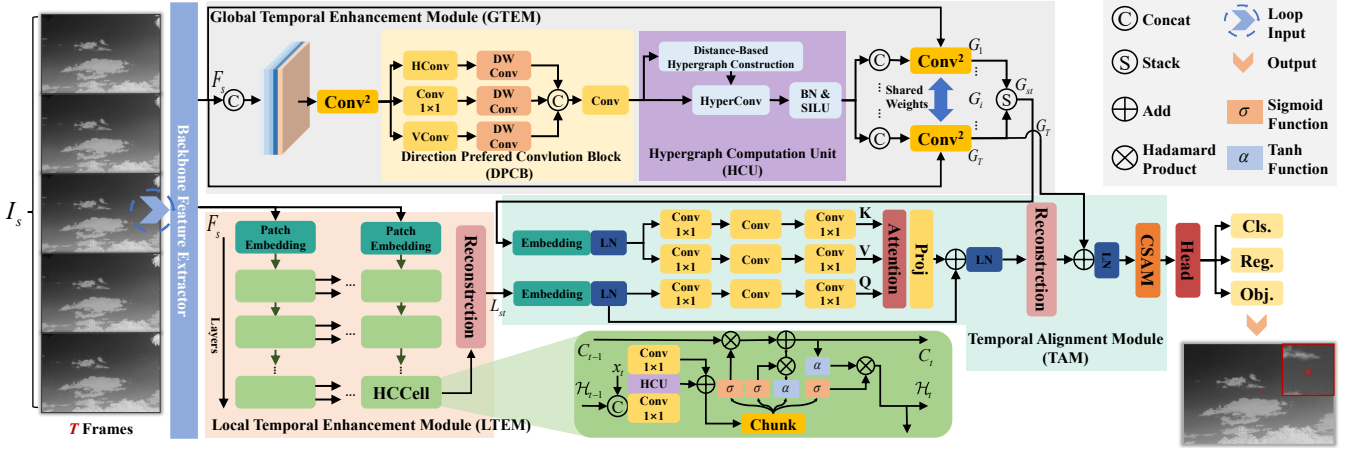


Fig. 1: Overview of the proposed framework HyperTea. Our HyperTea consists of a backbone and three key modules: the global temporal enhancement module, local temporal enhancement module, and temporal alignment module. I_s is T consecutive frames. It is fed into backbone to get spatial feature F_s . GTEM and LTEM enhance F_s at global and local temporal scales respectively, yielding G_{st} and L_{st} . Then G_{st} and L_{st} are aligned by TAM to generate F_{gt} . Finally, the fully fused features F_{gt} are fed into the detection head.

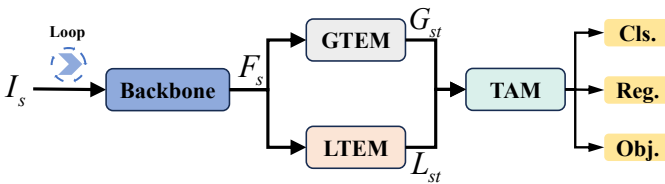


Fig. 2: Simplified workflow of our HyperTea. It contains the calculation process of input I_s and the feature flow of target detection.

C. Global Temporal Enhancement Module

Enhancing global temporal context through inter-frame dependencies remains a challenging problem in MIRSTD. Previous approaches usually use the attention mechanism to model spatial dependencies [49] or inter-channel semantic dependencies [48]. However, since the attention mechanism essentially models the image as a fully connected graph, the limited representation capability hinders higher-order dependency learning. Recently, global-local semantic interactions have emerged as an effective paradigm for feature enhancement [18], [23]. Inspired by these, we propose GTEM as shown in Figure 1, which includes temporal feature aggregation, direction-preferred convolution, higher-order association learning, and global semantic scattering mechanism.

Specifically, we first aggregate global temporal feature through two convolution layers.

$$\mathbf{L}_{gt} = \text{Conv}_{3 \times 3}^2(\text{Concat}[\mathbf{F}_1, \dots, \mathbf{F}_T]) \quad (3)$$

where $\text{Conv}_{3 \times 3}^2$ means two 3×3 basic convolution components with batch normalization and an activation layer.

In practice, features of background clutters often exhibit striped or bar-like patterns corresponding to physical objects. Therefore, We design a Direction-Preferred Convolution Block (DPCB) to encode such discriminative features into the channel dimension to enhance the feature representation, as shown

in Figure 1. In terms of implementation, we use convolution with kernel sizes 1×5 , 5×1 , 1×1 respectively to extract features with different direction preferences. Then 3×3 basic depth-wise convolution components are used to enhance the local spatial features and expand the receptive field. After that we apply 3×3 convolution to fuse the extracted features and obtain D_{gt} .

$$\begin{cases} \mathbf{L}_h = \text{DWC}(\text{Conv}_{1 \times 5}(\mathbf{L}_{gt})) \\ \mathbf{L}_v = \text{DWC}(\text{Conv}_{5 \times 1}(\mathbf{L}_{gt})) \\ \mathbf{L}_s = \text{DWC}(\text{Conv}_{1 \times 1}(\mathbf{L}_{gt})) \\ \mathbf{D}_{gt} = \text{Conv}_{3 \times 3}(\text{Concat}[\mathbf{L}_h, \mathbf{L}_v, \mathbf{L}_s]) + \mathbf{L}_{gt} \end{cases} \quad (4)$$

where DWC stands for 3×3 depth-wise convolution, $\mathbf{L}_h, \mathbf{L}_v, \mathbf{L}_s$ represent features with horizontal direction preference, vertical direction preference, and no directional preference, respectively.

Subsequently, HCU receives D_{gt} as its input and generates higher-order semantic-enhanced feature G_h . Then, in order to enhance global temporal context through G_h , we propagate G_h to each time step via convolution layers with shared weights. The global temporal enhanced features G_{st} thus can be obtained as follows:

$$\mathbf{G}_h = \text{HCU}(\mathbf{D}_{gt}) \quad (5)$$

$$\mathbf{G}_i = \text{Conv}_{3 \times 3}^2(\text{Concat}[\mathbf{F}_i, \mathbf{G}_h]), i = 1, \dots, T \quad (6)$$

D. Local Temporal Enhancement Module

In order to achieve robust and accurate detection on keyframe, we believe that it is crucial to effectively model local motion patterns, especially when dealing with dynamic complex scenes. Considering the powerful capability of convLSTM [15] and their variants [53], [54], [9], [21] in spatiotemporal representation learning, also combining HGNNs' advantages of higher-order learning, we design Hypergraph Convolution LSTM and its basic Cell (HCCell). In HCCell,

higher-order messages can be propagated between different gates in a common semantic space, which greatly enhances its local spatiotemporal feature learning capability.

Specifically, we made the following improvements based on the ConvLSTM node. As shown in Figure 1, we first project the input \mathcal{X}_t and hidden state \mathcal{H}_{t-1} into the same semantic space via 1×1 convolution. Then, we perform high-order semantic enhancement by HCU to obtain the enhanced feature \mathcal{L}_h . Subsequently, we apply convolution with residual connections to achieve semantic modulation of \mathcal{L}_h and obtain \mathcal{F}_t . After that, we split \mathcal{F}_t along the channel dimension and then apply corresponding activation functions to finally obtain four gates. The computational model of the HCell mathematically follows:

$$\begin{cases} \mathcal{L}_h = \text{HCU}(\text{Conv}_{1 \times 1}([\mathcal{X}_t, \mathcal{H}_{t-1}])) \\ \mathcal{F}_t = \text{Conv}_{1 \times 1}(\mathcal{L}_h) + \mathcal{L}_h \\ i_t, f_t, o_t, g_t = \text{Act}(\text{Chunk}(\mathcal{F}_t)) \\ \mathcal{C}_t = f_t \circ \mathcal{C}_{t-1} + i_t \circ g_t \\ \mathcal{H}_t = o_t \circ \tanh(\mathcal{C}_t) \end{cases} \quad (7)$$

where Act uses the sigmoid function to activate i_t, f_t, o_t and the tanh function for g_t , and \circ denotes the Hadamard (element) product.

E. Temporal Alignment Module

Our approach utilizes different branches to explore the global and local spatiotemporal features representations of infrared targets. However, the relative motion between target and imaging platform along with the learning path differences often lead to feature misalignment between global and local spatiotemporal features. To address this, we propose TAM as illustrated in Figure 1, which consists of global-local temporal attention (GLTA) and channel spatial aggregation module (CSAM).

1) Global-Local Temporal Attention: Specifically, we first perform patch embedding and layer normalization on global temporal context-enhanced feature \mathbf{G}_{st} , local temporal context-enhanced feature \mathbf{L}_{st} .

$$\hat{\mathbf{G}}_{st} = \text{LN}(\text{EMD}(\mathbf{G}_{st})) \quad (8)$$

$$\hat{\mathbf{L}}_{st} = \text{LN}(\text{EMD}(\mathbf{L}_{st})) \quad (9)$$

Subsequently, we use 1×1 convolution to project \mathbf{G}_{st} and \mathbf{L}_{st} into semantic spaces with the same dimensions. Then, in order to fuse features at different temporal scales, our GLTA employs \mathbf{L}_{st} as query, \mathbf{G}_{st} as key and value to realize fine-grained feature fusion.

$$\mathbf{Q} = \text{Conv}_{1 \times 1}(\text{Conv}_{3 \times 3}(\text{Conv}_{1 \times 1}(\hat{\mathbf{L}}_{st}))) \quad (10)$$

$$\mathbf{K} = \text{Conv}_{1 \times 1}(\text{Conv}_{3 \times 3}(\text{Conv}_{1 \times 1}(\hat{\mathbf{G}}_{st}))) \quad (11)$$

$$\mathbf{V} = \text{Conv}_{1 \times 1}(\text{Conv}_{3 \times 3}(\text{Conv}_{1 \times 1}(\hat{\mathbf{G}}_{st}))) \quad (12)$$

$$\text{Attn} = \text{Softmax}\left(\frac{\mathbf{Q}\mathbf{K}^T}{\sqrt{d}}\right)\mathbf{V} \quad (13)$$

where \sqrt{d} is a normalised scale factor. In this way, any two pixels can interact and cross-temporal dependencies between

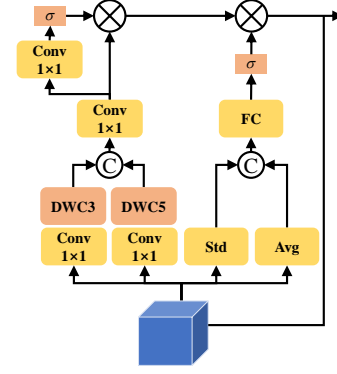


Fig. 3: Details of our proposed CSAM.

them can be captured, rather than being confined solely to the current temporal scale.

In addition, with the aim of preserving more original information, we also incorporate residual blocks to embed keyframe features at different temporal scales into the query results \mathbf{R} :

$$\mathbf{R} = \text{LN}(\mathbf{G}_T + \text{UP}(\text{LN}(\text{Conv}_{1 \times 1}(\text{Attn}) + \hat{\mathbf{L}}_{st}))) \quad (14)$$

where LN is layer normalization, UP denotes the reconstruct layer consists of a upsample layer and a convolution layer.

2) Channel Spatial Aggregation Module: Recently, leveraging channel and spatial global information has become a common practice in feature enhancement. Inspired by [8], [18], we design CSAM to further optimize the selection of spatial and channel weights.

As shown in Figure 3, given an input tensor $\mathbf{X} \in \mathbb{R}^{C \times H \times W}$, CSAM first adjusts the channel dimension by 1×1 convolution and employs 3×3 and 5×5 depth-wise convolution to enhance the local spatial information. And then CSAM compress the channel dimension to 1 to obtain the spatial attention map \mathbf{X}_{sa} . The above process can be formulated as:

$$\mathbf{X}_s = f_1^c([f_3^{dwc}(f_1^c(\mathbf{X})), f_5^{dwc}(f_1^c(\mathbf{X}))]) \quad (15)$$

$$\mathbf{X}_{sa} = f_{sa}^c(\mathbf{X}_s) \odot \mathbf{X}_s \quad (16)$$

where f_1^c denotes 1×1 convolution, f_3^{dwc} and f_5^{dwc} represent 3×3 and 5×5 depth-wise convolutions, f_{sa}^c stands for 1×1 convolution whose output channel is 1 with sigmoid activation function, \odot is the broadcasted Hadamard product.

Then, to better estimate the weights of different channels, we compute the maximum value and standard deviation of each channel and further use learnable parameters to obtain channel weights \mathbf{X}_{ca} as follows:

$$\mathbf{X}_{ca} = fc([\max(\mathbf{X}), \text{std}(\mathbf{X})]) \quad (17)$$

where fc denotes a linear transform layer with sigmoid activation function. At last, CSAM enriches the representation of features by integrating complementary spatial and channel information with residual concatenation.

$$\mathbf{X}_{sc} = \mathbf{X}_{ca} \odot \mathbf{X}_{sa} + \mathbf{X} \quad (18)$$

F. Loss Function

Following the general detection paradigm [52], [9], a traditional loss function can be defined as follows:

$$\mathcal{L} = \lambda_{\text{reg}}\mathcal{L}_{\text{reg}} + \lambda_{\text{cls}}\mathcal{L}_{\text{cls}} + \lambda_{\text{obj}}\mathcal{L}_{\text{obj}} \quad (19)$$

where \mathcal{L}_{reg} is the bounding box regression loss, \mathcal{L}_{cls} is the classification loss, and \mathcal{L}_{obj} is the target probability loss. λ_{reg} , λ_{cls} , λ_{obj} are the hyperparameters that balance the loss terms. For \mathcal{L}_{cls} and \mathcal{L}_{obj} , we use binary cross-entropy loss function. Hyperparameters and \mathcal{L}_{reg} follow [49].

IV. EXPERIMENTS

A. Datasets and Evaluation Metrics

In order to fully validate the effectiveness and superiority of our HyperTea, we conduct experiments on two datasets, DAUB [60] and IRDST [34]. The division of datasets follows [9].

In terms of evaluation metrics, we follow the widely adopted practice in the object detection paradigm [52] and adopt precision (Pr), recall (Re), F1-score, and mean Average Precision at an IoU threshold of 0.5 (mAP₅₀). These metrics are defined as follows:

$$\text{Precision} = \frac{\text{TP}}{\text{TP} + \text{FP}}, \quad (20)$$

$$\text{Recall} = \frac{\text{TP}}{\text{TP} + \text{FN}}, \quad (21)$$

$$\text{F1} = \frac{2 \times \text{Precision} \times \text{Recall}}{\text{Precision} + \text{Recall}}, \quad (22)$$

where TP, FP, and FN denote the number of true positives (correctly detected targets), false positives (background regions incorrectly identified as targets), and false negatives (missed targets), respectively. The F1-score serves as a harmonic mean of precision and recall, providing a balanced measure that jointly evaluates a detector’s ability to minimize both missed detections and false alarms.

B. Implementation Details

The input frame resolution is reshaped to 512×512 in all experiments. All methods are trained for 50 epochs with a batch size of 4. We set initial learning rate to 0.01, and adopt SGD as the optimizer with momentum 0.937, weight decay 5×10^{-4} , and learning rate reduction factor 0.1. For non-maximal suppression, the IoU threshold is set to 0.65, while the confidence threshold is 0.001. We performed all experiments on one Nvidia GeForce 4090D GPU.

C. Comparisons With Other Methods

1) *Quantitative Comparison*: Considering that learning-based methods tend to have much more superior detection performance compared to model-based ones, we select some state-of-the-art learning-based IRSTD methods for comparison. For segmentation-based methods, we follow the paradigm of combined detector [9], [49].

The quantitative performance of different detection methods on two datasets is clearly shown in Table I. Based on the data

in Table I, three important findings can be identified. First, the detection performance of single-frame methods is typically inferior to that of multi-frame methods; however, they may outperform certain multi-frame approaches when temporal associations within the dataset are challenging to exploit. For instance, on DAUB, the SOTA single-frame method, MSHNet achieves an mAP₅₀ of 85.25% and an F1 score of 92.56%, which are lower than any multi-frame method listed in Table I. That’s because single-frame methods rely solely on spatial features, thereby limiting their capacity to adaptively capture the temporal dynamics of targets. However, on IRDST, the leading single-frame method, DNANet, attains an mAP₅₀ of 71.39% and an F1 score of 84.86%, surpassing the multi-frame methods TMP and SSTNet. This may be attributed to the more complex temporal associations in IRDST compared to DAUB. To quantify inter-frame similarity, we employed the mean squared error (MSE) metric, calculating an average MSE of 32.95 for DAUB and 112.03 for IRDST. The higher MSE in IRDST indicates greater complexity in temporal relationships, suggesting that under such conditions, the limited ability of some multi-frame methods to effectively leverage temporal associations may result in their performance being outstripped by single-frame approaches.

Second, our Hypertea achieves the best performance on most evaluation metrics on both datasets, particularly in terms of mAP₅₀ and F1 score. For instance, on DAUB, Hypertea attains the highest mAP₅₀ of 95.59% and the highest F1 score of 98.23%. Furthermore, on IRDST, our Hypertea still achieves the highest mAP₅₀ of 76.42% and F1 score of 87.62%, far outperforming the previous state-of-the-art (SOTA) method Tridos, which delivers an mAP₅₀ of 72.54% and an F1 score of 85.63%.

Third, our HyperTea exhibits stronger temporal feature extraction capability, making it more suitable for complex imaging scenarios. Since samples in DAUB are relatively stable in the temporal domain, all multi-frame methods perform better on DAUB than on IRDST. For example, the previous multi-frame SOTA method Tridos achieves an mAP₅₀ of 91.52% and an F1 score of 96.17% on DAUB, but only reaches an mAP₅₀ of 72.54% and an F1 score of 85.63% on IRDST. Nevertheless, on DAUB, our HyperTea achieves a 4.07% mAP₅₀ improvement and a 2.06% F1 score improvement over Tridos. On IRDST, the improvement of HyperTea is still significant, with mAP₅₀ and F1 score increments over Tridos reaching 3.88% and 1.99%, respectively. These comparisons indicate that compared with other methods, HyperTea can more effectively adapt to dynamic temporal scenarios and extract complex temporal features for detection.

2) *Visual Comparison*: To provide an intuitive visualization of the detection performances of different methods, we choose three representative scenarios for demonstration, as shown in Figures 4 to 6. It can be observed that our HyperTea consistently achieves accurate detection of moving infrared small targets. By contrast, other methods tend to suffer from missed detections or false alarms.

For example, in Figure 4, on IRDST, our hypertea can accurately detect target in complex scenarios with substantial cloud clutters. In contrast, many other methods like ACM,

TABLE I: Comparisons with state-of-the-art methods on four metrics: mAP₅₀, Precision, Recall, and F1.

Scheme	Methods	Publication	IRDST				DAUB			
			mAP ₅₀	Pr	Re	F1	mAP ₅₀	Pr	Re	F1
single-frame	ACM [7]	WACV 2021	65.31	82.11	80.70	81.40	83.41	93.11	90.65	91.86
	ALC [55]	TGRS 2021	53.10	77.30	69.03	72.93	79.03	90.41	88.43	89.40
	ISNet [33]	CVPR 2022	66.30	84.24	79.80	81.96	83.02	93.52	89.99	91.72
	AGPCNet [17]	TAES 2023	67.10	85.40	79.74	82.47	82.43	90.17	92.62	91.38
	MTUNet [56]	TGRS 2023	67.20	86.35	78.70	82.35	77.21	93.40	83.42	88.13
	DNANet [8]	TIP 2023	71.39	88.36	81.63	84.86	84.44	97.37	87.34	92.08
	RDIANet [34]	TGRS 2023	68.70	85.29	81.86	83.54	80.72	88.29	92.95	90.56
	MSHNet [57]	CVPR 2024	71.04	87.92	81.89	84.80	85.25	99.30	86.67	92.56
	SCTransNet [18]	TGRS 2024	68.41	82.93	83.08	83.01	79.97	94.34	85.99	89.97
	RPCANet [58]	WACV 2024	68.80	84.41	82.29	83.33	78.90	82.85	96.93	89.34
SeRankDet [59]	TGRS 2024	69.50	86.16	81.38	83.70	84.67	94.60	90.47	92.49	
multi-frame	DTUM [47]	TNNLS 2023	71.80	85.12	85.36	85.24	90.46	97.86	93.58	95.67
	SSTNet [9]	TGRS 2024	70.91	87.73	81.98	84.76	89.07	97.12	92.72	94.87
	TMP [48]	ESWA 2024	69.12	86.57	80.99	83.68	85.37	94.23	91.74	92.96
	Tridos [49]	TGRS 2024	72.54	87.82	83.63	85.63	91.52	96.83	95.52	96.17
	HyperTea(Ours)	-	76.42	91.18	84.33	87.62	95.59	98.14	98.31	98.23

DNANet, RDIAN, SCTransNet, DTUM, SSTNet, and TMP tend to misclassify clutters as targets. Furthermore, in Figure 5, when targets are surrounded by cloud clutters, some methods fail to avoid clutter interference and erroneously identify clutters as targets, including DNANet, RDIAN, SCTransNet, DTUM, and TMP. Meanwhile, as shown in Figure 6, on DAUB, some methods struggle to detect extremely small targets amid complex backgrounds, such as ISNet, MSHNet, SeRankDet, and TMP. Other methods, however, result in false alarms, including ACM, AGPCNet, DTUM, and Tridos. In summary, the visualization results in these typical scenarios are highly consistent with the quantitative performance presented in Table I, thereby demonstrating the superiority of our Hyperteas.

3) *PR Curve Comparison*: To visually assess the overall performance of different methods, we plot two PR curves on DAUB and IRDST, as shown in Figure 7. It is readily observable that the PR curve of our Hyperteas nearly envelops those of other methods on both datasets. On DAUB, Hyperteas’s curve consistently dominates the upper-right region relative to competitors; remarkably, it maintains high precision even at relatively high recall. On IRDST, Hyperteas’s PR curve almost invariably lies above those of other methods. In PR curve analysis, a curve closer to the upper-right corner indicates a superior balance between detection precision and recall. Thus, these two sets of PR curves collectively demonstrate that our Hyperteas achieves optimal overall detection performance compared to other methods.

4) *Model Complexity Comparison*: We compare the model complexity of Hyperteas with 15 representative methods in Table II, focusing on Params, GFlops, and frames persecond (FPS). Two key observations emerge from the table.

One is that Hyperteas exhibits a slight increase in Params and GFlops. Among multi-frame methods, DTUM has the smallest params at 2.79M, while Hyperteas has a moderate 13.75M, lower than TMP (16.41M) and Tridos (14.13M). In terms of GFlops, TMP achieves the best result among multi-frame methods at 92.85%, whereas Hyperteas registers 148.66.

A probable reason is that TMP based on a single temporal scale, while Hyperteas learns feature representations across both local and global temporal scales and requires cross-scale alignment, which entails additional computations. Nevertheless, these complexity costs are acceptable and worthwhile given Hyperteas’s significant performance advantages.

The other observation is that Hyperteas achieves an excellent balance between performance and FPS. Since multi-frame methods based on spatiotemporal domains, they typically outperform single-frame methods in performance but often have lower FPS. For instance, DNANet, the SOTA single-frame method, whose F1 score of 84.86%—roughly on par with SSTNet’s 84.76%, but far below Hyperteas’s 87.62%. And its FPS 12.13 is also lower than Hyperteas’s 14.52. Moreover, among multi-frame methods, Hyperteas boasts the highest FPS, even surpassing some single-frame methods such as DNANet and SCTransNet. This underscores its superior balance between detection performance and inference efficiency.

TABLE II: Complexity comparisons of inference on IRDST.

Methods	Frames	mAP ₅₀ ↑	F1 ↑	Params ↓	GFlops ↓	FPS ↑
ACM [7]	1	65.31	81.40	2.89M	24.14	51.55
ALC [55]	1	53.10	72.93	2.92M	23.95	56.23
AGPCNet [17]	1	67.10	82.47	14.85M	366.37	15.72
MTUNet [56]	1	67.20	82.35	9.13M	67.42	48.79
ISNet [33]	1	66.30	81.96	3.46M	265.87	26.82
DNANet [8]	1	71.39	84.86	7.19M	135.00	12.13
RDIANet [34]	1	68.70	83.54	2.71M	50.67	45.64
MSHNet [57]	1	71.04	84.80	6.55M	69.78	25.73
SCTransNet [18]	1	68.41	83.01	35.74M	147.02	14.22
RPCANet [58]	1	68.80	83.33	3.17M	377.48	26.40
SeRankDet [59]	1	69.50	83.70	111.37M	1147	18.54
DTUM [47]	5	71.80	85.24	2.79M	103.73	12.85
SSTNet [9]	5	70.91	84.76	11.95M	123.60	12.97
TMP [48]	5	69.12	83.68	16.41M	92.85	14.02
Tridos [49]	5	72.54	85.63	14.13M	130.72	13.24
HyperTea1(Ours)	5	76.42	87.62	13.75M	148.66	14.52

D. Ablation Study

1) *Effects of Different Components*: To investigate the effectiveness of each component in HyperTeas, we conducted a series of ablation studies on DAUB and IRDST, as shown in Table III. For the ablation experiments of TAM, we use

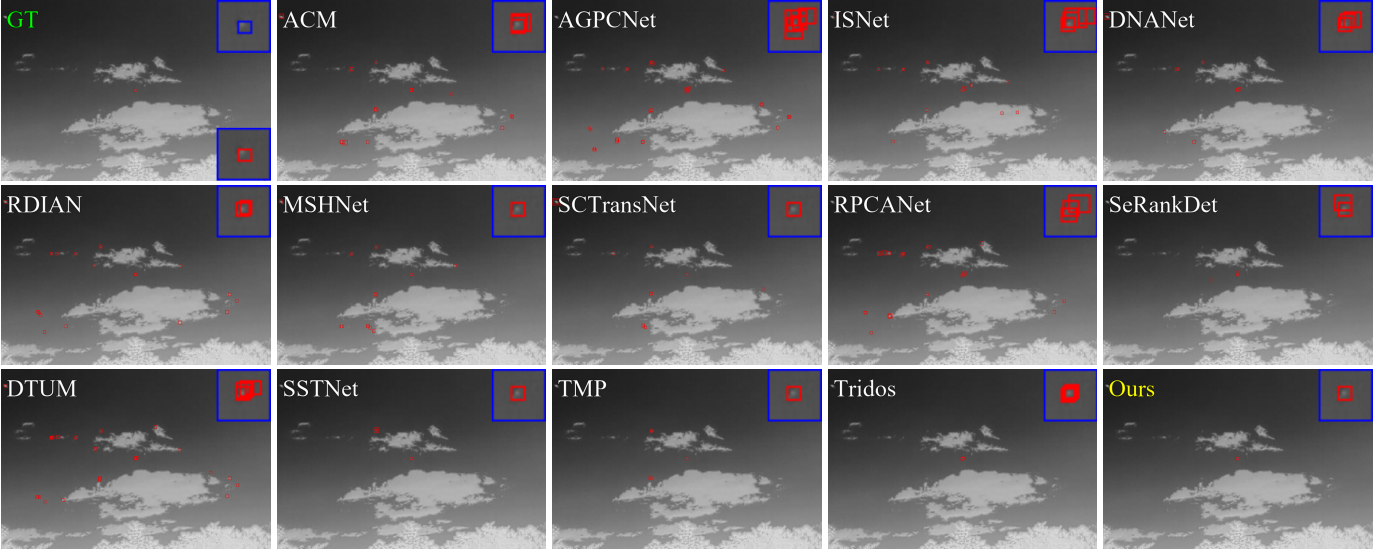


Fig. 4: Visualization comparisons of 14 methods on IRDST, with 72/266.bmp. GT is ground truth. Red and blue boxes represent detected targets and amplified detection regions, respectively.

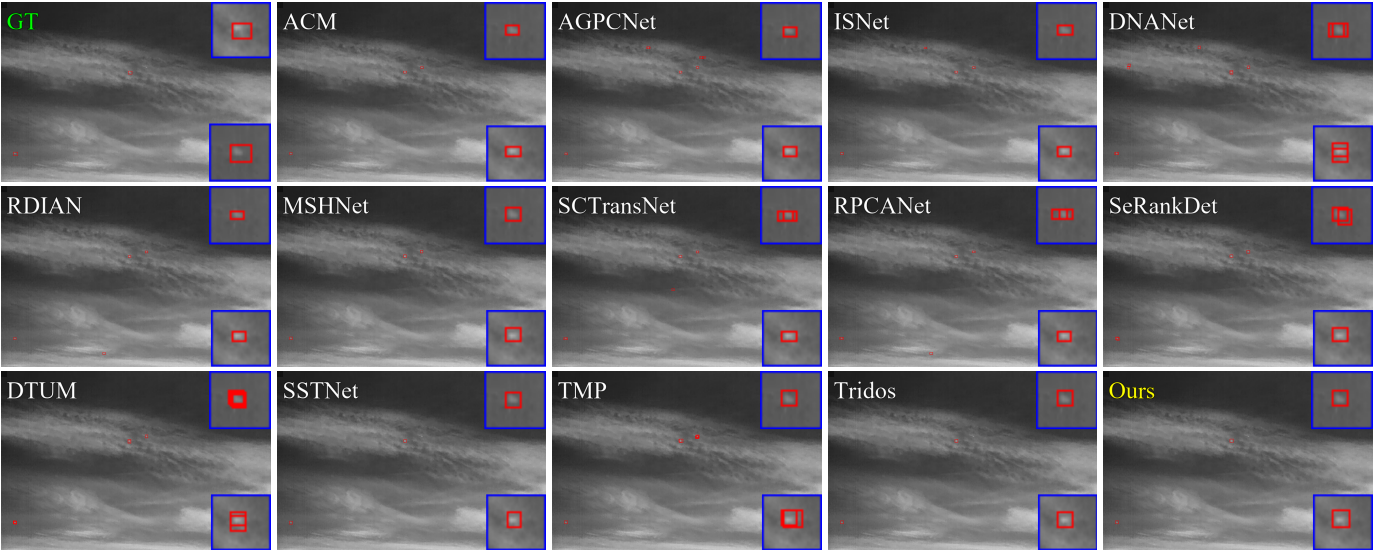


Fig. 5: Visualization comparisons of 14 methods on IRDST, with 6/14.bmp. GT is ground truth. Red and blue boxes represent detected targets and amplified detection regions, respectively.

1×1 convolutions to adjust the number of channels, aiming to verify the module’s effectiveness while minimizing changes to the network structure.

Two key findings can be drawn from Table III. First, each component contributes to improving detection performance to some extent, and the best performance is achieved when all components are applied together. For example, on IRDST, the baseline without any components only achieves an mAP_{50} of 66.80% and an F1 score of 81.94%. After applying LTEM alone, the mAP_{50} increases to 69.42% and the F1 score to 83.55%. When GTEM is applied alone, the mAP_{50} and F1 score are further improved to 71.44% and 84.99%, respectively. Additionally, the performance of TAM varies with different inputs. When features enhanced by both LTEM and GTEM are fed into TAM, the mAP_{50} and F1 score on DAUB

increase to 95.59% and 98.23%, respectively; on IRDST, they reach 76.42% and 87.62%, achieving the best performance. Second, simple 1×1 convolutions fail to effectively realize cross-temporal feature fusion. For instance, on IRDST, the model without TAM only achieves an mAP_{50} of 69.07% and an F1 score of 83.25%, which is lower than those of the model with LTEM alone (mAP_{50} : 69.42%, F1: 83.55%) and the model with GTEM alone (mAP_{50} : 71.44%, F1: 84.99%).

2) *Effects of DPCB and HCU in GTEM*: To explore the potential contributions of HCU and DPCB to GTEM, we conducted a set of ablation experiments, as shown in Table IV. First, DPCB provides more robust feature representations by fusing multi-directional features, thereby improving detection performance. For example, with DPCB, on DAUB, mAP_{50} and F1 can be increased from 91.06% to 92.52% and from

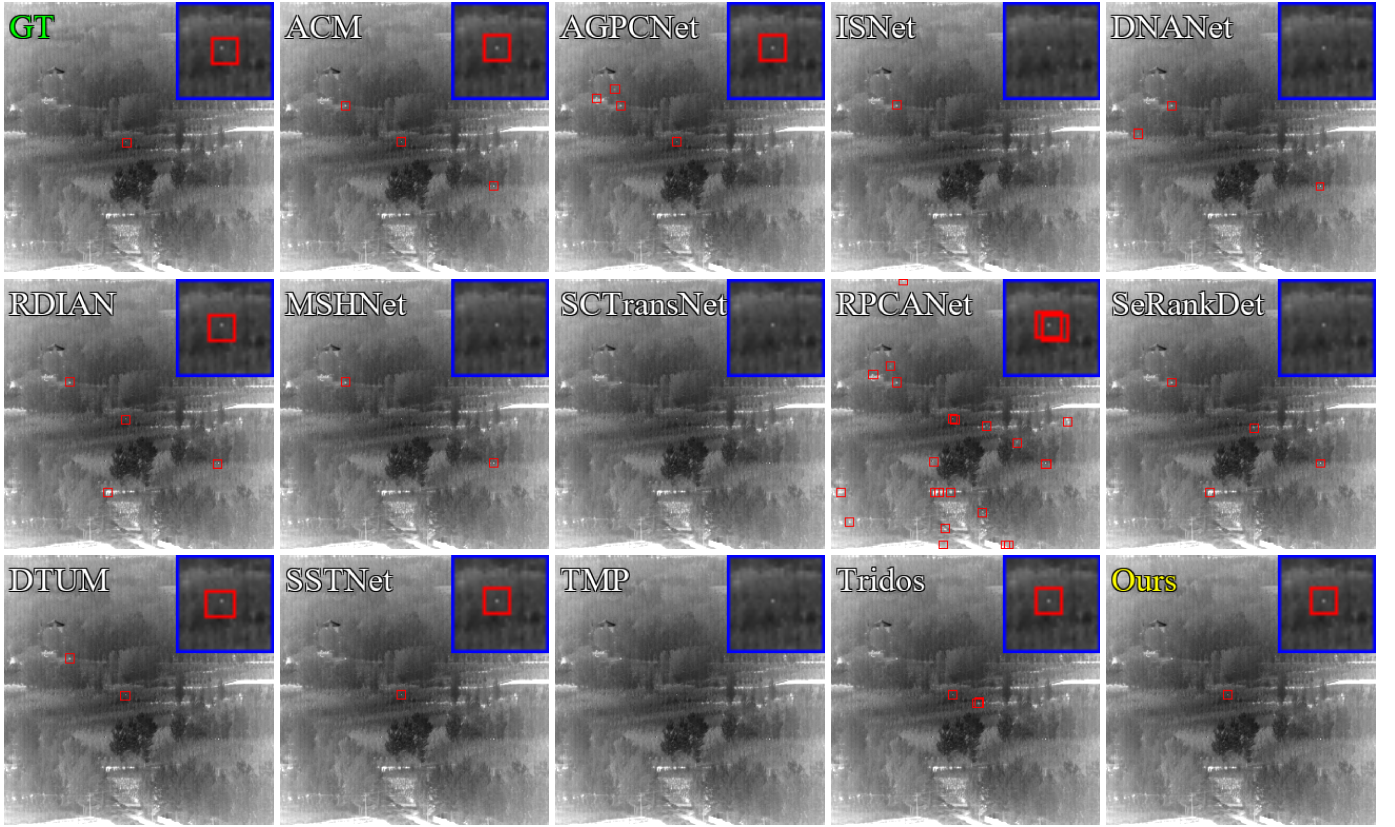


Fig. 6: Visualization comparisons of 14 methods on DAUB, with 21/433.bmp. GT is ground truth. Red and blue boxes represent detected targets and amplified detection regions, respectively.

TABLE III: Ablation study on different components. TAM(A) uses L_{st} as query and F_s as key & value. TAM(B) uses F_T as query and G_{st} as key & value.

Settings	LTEM	GTEM	TAM	IRDST				DAUB			
				mAP ₅₀	Pr	Re	F1	mAP ₅₀	Pr	Re	F1
w/o All	-	-	-	66.80	84.95	79.13	81.94	82.63	95.51	87.32	91.23
w/ LTEM	✓	-	-	69.42	88.01	79.52	83.55	89.05	94.47	95.95	95.21
w/ GTEM	-	✓	-	71.44	88.28	81.93	84.99	89.79	96.97	93.82	95.37
w/ LTEM & GTEM	✓	✓	-	69.07	86.67	80.09	83.25	89.74	97.84	92.67	95.19
w/ TAM(A)	✓	-	✓	72.18	89.25	81.66	85.28	90.92	96.18	95.45	95.81
w/ TAM(B)	-	✓	✓	73.27	89.49	82.52	85.86	91.05	95.53	96.66	96.09
Ours	✓	✓	✓	76.42	91.18	84.33	87.62	95.59	98.14	98.31	98.23

95.91% to 96.68%, respectively. Similarly, on IRDST, HCU can boost mAP₅₀ from 69.67% to 71.84% and F1 from 83.75% to 85.11%. These effects can be attributed to HCU’s strong capability in modeling high-order correlations.

3) *Effects of GLTA and CSAM in TAM*: In addition, we investigate the impacts of GLTA and CSAM in Table V, from which three distinct findings can be derived. First, GLTA effectively aligns the features enhanced by LTEM and GTEM. For instance, on DAUB, with GLTA, mAP₅₀ and F1 are improved from 89.74% to 92.13% and from 95.19% to 96.61%, respectively. Second, CSAM can further enhance the aligned features. On IRDST, for example, using CSAM boosts mAP₅₀ from 73.30% to 76.42% and F1 from 85.85% to 87.62%. Third, the performance gain from using CSAM alone is limited. On DAUB, for instance, with CSAM alone merely increases mAP₅₀ from 89.74% to 89.81% and F1 from

95.19% to 95.23%. This phenomenon also reflects the severe impact of misalignment between features of different temporal scales on detection performance.

TABLE IV: Ablation study on DPCB and HCU of GTEM.

Settings	IRDST				DAUB			
	mAP ₅₀	Pr	Re	F1	mAP ₅₀	Pr	Re	F1
GTEM w/o All	69.67	87.15	80.61	83.75	91.06	97.22	94.64	95.91
GTEM w HCU	71.84	88.76	81.76	85.11	92.33	97.59	95.55	96.56
GTEM w DPCB	71.99	89.07	81.78	85.27	92.52	96.13	97.24	96.68
GTEM	76.42	91.18	84.33	87.62	95.59	98.14	98.31	98.23

TABLE V: Ablation study on GLTA and CSAM of TAM.

Settings	IRDST				DAUB			
	mAP ₅₀	Pr	Re	F1	mAP ₅₀	Pr	Re	F1
TAM w/o All	69.07	86.67	80.09	83.25	89.74	97.84	92.67	95.19
TAM w GLTA	73.30	88.76	83.13	85.85	92.13	95.73	97.52	96.61
TAM w CSAM	69.78	87.36	80.81	83.96	89.81	95.08	95.39	95.23
TAM	76.42	91.16	84.28	87.62	95.59	98.14	98.31	98.23

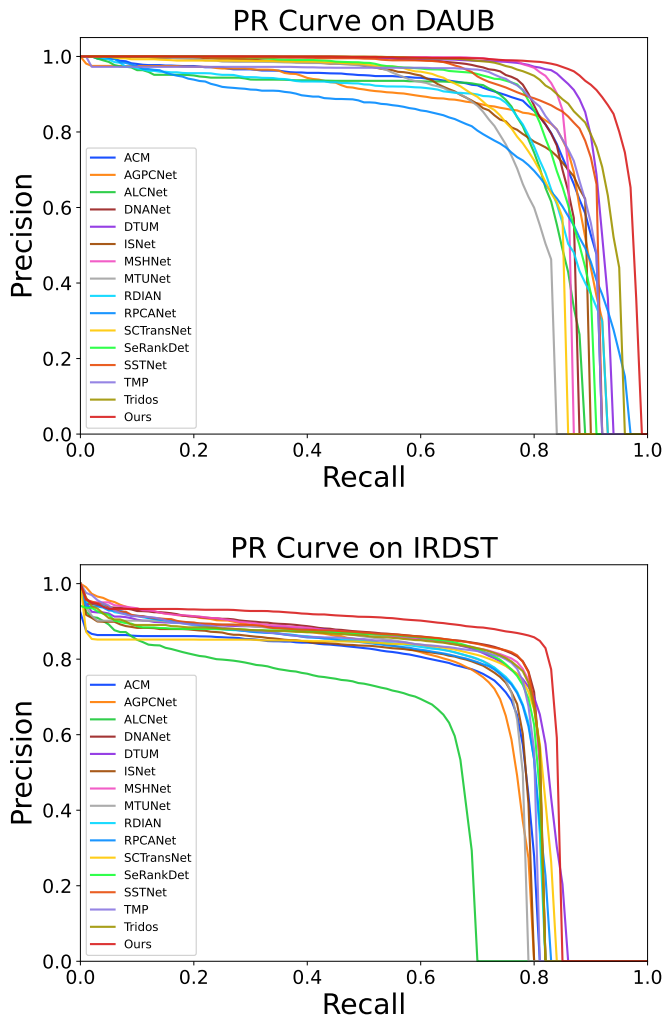


Fig. 7: PR curves of 16 representative detection methods on datasets DAUB and IRDST.

4) *Effects of layer number and patch size in LTEM*: As shown in Table VI, we designed six sets of experiments to evaluate the impact of layers number (L) and patch size (ps) on LTEM. From these experiments, we can draw the following three observations. First, when $L=1$ and $ps=2$, the mAP_{50} on DAUB and IRDST can reach peak values of 95.59% and 76.42%, respectively. In the experiments, any other settings generally fail to enable HyperTea to achieve the optimal performance. Second, when the number of layers increases, HyperTea exhibits a significant performance degradation on both DAUB and IRDST. For example, on DAUB, when L increases from 1 to 2, mAP_{50} drops from 95.59% to 88.07%. A possible reason for this observation is that HyperTea suffers from overfitting when the number of layers is greater than 1. Third, performance degrades when ps is too small or too large. For instance, on DAUB, $L=1$, when ps decreases from 2 to 1, mAP_{50} drops from 95.59% to 92.31%; when ps increases from 2 to 4, mAP_{50} decreases from 95.59% to 93.04%. A possible reason for this observation is that when $ps=1$, the semantic features of a single pixel are insufficient to effectively model long-range dependencies; when $ps=4$, an excessively

large size leads to the loss of low-level details. Only when $ps=2$ can the optimal performance be achieved by enriching feature representations while well preserving low-level details.

TABLE VI: With different layer number L and patch size ps of LTEM.

L	ps	IRDST				DAUB			
		mAP_{50}	Pr	Re	F1	mAP_{50}	Pr	Re	F1
1	1	71.83	88.78	81.74	85.11	92.31	95.90	97.64	96.76
1	2	76.42	91.18	84.33	87.62	95.59	98.14	98.31	98.23
1	4	69.80	88.54	79.66	83.87	93.04	96.67	97.22	96.94
2	1	70.27	87.96	80.84	84.25	89.68	93.22	97.41	95.27
2	2	71.69	88.70	81.49	84.94	88.07	92.47	96.28	94.34
2	4	71.06	89.10	80.20	84.41	92.34	95.95	97.83	96.88

TABLE VII: With different hypergraph distance threshold.

Settings	IRDST				DAUB			
	mAP_{50}	Pr	Re	F1	mAP_{50}	Pr	Re	F1
6	72.14	88.36	82.24	85.19	93.25	95.99	98.22	97.09
7	72.96	89.01	82.85	85.82	92.86	96.36	97.93	97.14
8	76.42	91.18	84.33	87.62	95.59	98.14	98.31	98.23
9	71.15	87.99	81.66	84.71	88.54	92.09	97.62	94.78
10	70.31	87.04	81.32	84.08	92.33	94.99	98.22	96.58

5) *Effects of Hypergraph distance threshold*: We further conducted ablation experiments to investigate the impact of the distance threshold used in hypergraph construction, with the results shown in Table VII. It can be observed that when the threshold is 8, the mAP_{50} on DAUB and IRDST reaches peak values of 95.59% and 76.42% respectively, and both excessively low and high thresholds lead to performance degradation. This is because a higher threshold result in more densely connected hypergraphs, where noisy nodes are mixed into hyperedges, potentially causing features to lack discriminability. In contrast, a lower threshold leads to sparser hypergraphs, preventing the high-order learning capability of the hypergraph from being fully utilized. Therefore, our HyperTea is constructed using a distance threshold of 8, with the exact value determined based on experience and experimental results.

6) *Effects of Time Window Size T* : We conduct a group of experiments with different time window sizes to investigate the impact of time window T on detection performance, as shown in Figure 8.

First, it can be observed that the impact of T on detection performance differs between DAUB and IRDST. On DAUB, HyperTea achieves peak mAP_{50} and F1 values when $T=3$. On IRDST, however, the peak mAP_{50} and F1 values are reached when $T=5$. The discrepancy in the T values corresponding to these peaks is mainly due to differences between the datasets. As mentioned earlier, the average MSE values of DAUB and IRDST are 32.95 and 112.03 respectively, meaning the temporal dynamics of IRDST are more complex, making the learning of its temporal features more challenging and thus requiring more frames. In contrast, the temporal dynamics of DAUB are relatively stable, so the temporal context provided by 3 frames is sufficient for detection.

Additionally, an appropriate T is crucial for IRDST. For example, on DAUB, when $T \leq 3$, increasing T leads to a noticeable improvement in performance. When $T > 3$, the detection performance first decreases and then fluctuates, showing an overall tendency to stabilize. This is consistent

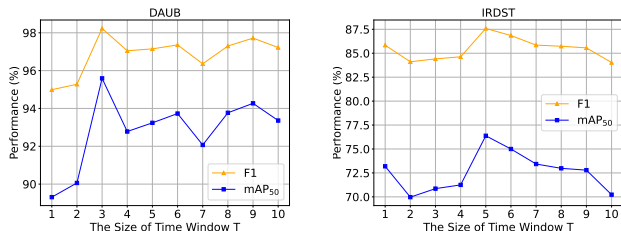


Fig. 8: Effects of time window size T on HyperTea.

with the temporal dynamic characteristics of DAUB: with smaller MSE, 3 frames are enough for detection, longer temporal context provides limited gains and may even risk performance degradation due to feature redundancy and clutter interference.

7) *Comparison With Hyper-YOLO*: To further verify the advantages of our HyperTea, we compared it with Hyper-YOLO, as shown in Table VII. It can be observed that our HyperTea has a significant leading advantage over Hyper-YOLO on both datasets. For instance, on DAUB, HyperTea attains an mAP₅₀ of 95.59%, Precision (Pr) of 98.14%, Recall (Re) of 98.31%, and F1 of 98.23%, which are far superior to those of Hyper-YOLO. This set of quantitative comparisons indicates that the main advantage of our proposed HyperTea lies in fully leveraging the complementary advantages between basic network structures and performing feature enhancement and alignment across different temporal scales, rather than simply integrating the hypergraph module into the detection framework.

TABLE VIII: PERFORMANCE COMPARISONS WITH Hyper-YOLO.

Methods	IRDST				DAUB			
	mAP ₅₀	Pr	Re	F1	mAP ₅₀	Pr	Re	F1
Hyper-YOLO	69.90	86.67	81.59	84.05	88.44	96.45	92.74	94.56
Ours	76.42	91.18	84.33	87.62	95.59	98.14	98.31	98.23

V. CONCLUSION

To achieve performance improvement by cross-temporal representation learning of moving infrared dim-small targets, we propose HyperTea, a network architecture combining CNNs, RNNs, and HGNNs. We first design a GTEM to enhance the global temporal context. Then, we develop the LTEM to enhance the local temporal context where key frames are located. Furthermore, we utilize HGNNs to endow GTEM and LTEM with the capability of high-order learning. To bridge potential feature misalignment, we design the TAM to facilitate the fusion of features across different temporal scales. Comparative experiments on DAUB and IRDST demonstrate the distinct superiority of our HyperTea. It outperforms existing state-of-the-art (SOTA) methods on most metrics, with moderate computational complexity and FPS. Ablation studies further indicate that all designed components contribute significantly to improving the detection performance. In experiments, we also find that the temporal similarity of datasets (measured by MSE) critically affects detection performance,

which should provide insights for the design of sampling strategies and modules using multi-frame inputs. In the future, designing more effective temporal feature sampling, capture, and enhancement schemes is worthy of ongoing exploration.

REFERENCES

- [1] R. Kou, C. Wang, Z. Peng, Z. Zhao, Y. Chen, J. Han, F. Huang, Y. Yu, and Q. Fu, "Infrared small target segmentation networks: A survey," *Pattern Recognition*, vol. 143, p. 109788, Nov. 2023.
- [2] C. L. P. Chen, H. Li, Y. Wei, T. Xia, and Y. Y. Tang, "A local contrast method for small infrared target detection," *IEEE Transactions on Geoscience and Remote Sensing*, vol. 52, no. 1, pp. 574–581, Jan. 2014.
- [3] M. Zeng, J. Li, and Z. Peng, "The design of top-hat morphological filter and application to infrared target detection," *Infrared Physics & Technology*, vol. 48, no. 1, pp. 67–76, Apr. 2006.
- [4] C. Gao, D. Meng, Y. Yang, Y. Wang, X. Zhou, and A. G. Hauptmann, "Infrared patch-image model for small target detection in a single image," *IEEE Transactions on Image Processing*, vol. 22, no. 12, pp. 4996–5009, Dec. 2013.
- [5] L. Zhang and Z. Peng, "Infrared small target detection based on partial sum of the tensor nuclear norm," *Remote Sensing*, vol. 11, no. 4, p. 382, Jan. 2019.
- [6] W. Gao, W. Niu, W. Lu, P. Wang, Z. Qi, X. Peng, and Z. Yang, "Dim small target detection and tracking: A novel method based on temporal energy selective scaling and trajectory association," *IEEE Journal of Selected Topics in Applied Earth Observations and Remote Sensing*, vol. 17, pp. 17239–17262.
- [7] Y. Dai, Y. Wu, F. Zhou, and K. Barnard, "Asymmetric contextual modulation for infrared small target detection," in *2021 IEEE Winter Conference on Applications of Computer Vision (WACV)*, Jan. 2021, pp. 949–958.
- [8] B. Li, C. Xiao, L. Wang, Y. Wang, Z. Lin, M. Li, W. An, and Y. Guo, "Dense nested attention network for infrared small target detection," *IEEE Transactions on Image Processing*, vol. 32, pp. 1745–1758, 2023.
- [9] S. Chen, L. Ji, J. Zhu, M. Ye, and X. Yao, "Sstnet: Sliced spatio-temporal network with cross-slice convlstm for moving infrared dim-small target detection," *IEEE Transactions on Geoscience and Remote Sensing*, vol. 62, pp. 1–12, 2024.
- [10] K. He, X. Zhang, S. Ren, and J. Sun, "Deep residual learning for image recognition," in *2016 IEEE Conference on Computer Vision and Pattern Recognition (CVPR)*. Las Vegas, NV, USA: IEEE, Jun. 2016, pp. 770–778.
- [11] A. Krizhevsky, I. Sutskever, and G. E. Hinton, "Imagenet classification with deep convolutional neural networks," *Commun. ACM*, vol. 60, no. 6, pp. 84–90, May 2017.
- [12] N. Carion, F. Massa, G. Synnaeve, N. Usunier, A. Kirillov, and S. Zagoruyko, "End-to-end object detection with transformers," Berlin, Heidelberg, Aug. 2020, pp. 213–229.
- [13] A. Dosovitskiy, L. Beyer, A. Kolesnikov, D. Weissenborn, X. Zhai, T. Unterthiner, M. Dehghani, M. Minderer, G. Heigold, S. Gelly, J. Uszkoreit, and N. Houlsby, "An image is worth 16x16 words: Transformers for image recognition at scale," in *International Conference on Learning Representations*, Oct. 2020.
- [14] Z. Liu, J. Ning, Y. Cao, Y. Wei, Z. Zhang, S. Lin, and H. Hu, "Video swin transformer," in *Proceedings of the IEEE/CVF Conference on Computer Vision and Pattern Recognition*, 2022, pp. 3202–3211.
- [15] X. SHI, Z. Chen, H. Wang, D.-Y. Yeung, W.-k. Wong, and W.-c. WOO, "Convolutional lstm network: A machine learning approach for precipitation nowcasting," in *Advances in Neural Information Processing Systems*, vol. 28, 2015.
- [16] X. Wu, D. Hong, and J. Chanussot, "Uiu-net: U-net in u-net for infrared small object detection," *IEEE Transactions on Image Processing*, vol. 32, pp. 364–376, 2023.
- [17] T. Zhang, L. Li, S. Cao, T. Pu, and Z. Peng, "Attention-guided pyramid context networks for detecting infrared small target under complex background," *IEEE Transactions on Aerospace and Electronic Systems*, vol. 59, no. 4, pp. 4250–4261, Aug. 2023.
- [18] S. Yuan, H. Qin, X. Yan, N. Akhtar, and A. Mian, "Sctransnet: Spatial-channel cross transformer network for infrared small target detection," *IEEE Transactions on Geoscience and Remote Sensing*, vol. 62, pp. 1–15, 2024.

- [19] X. Tong, Z. Zuo, S. Su, J. Wei, X. Sun, P. Wu, and Z. Zhao, "St-trans: Spatial-temporal transformer for infrared small target detection in sequential images," *IEEE Transactions on Geoscience and Remote Sensing*, vol. 62, pp. 1–19, 2024.
- [20] J. Lin, S. Li, L. Zhang, X. Yang, B. Yan, and Z. Meng, "Ir-transdet: Infrared dim and small target detection with ir-transformer," *IEEE Transactions on Geoscience and Remote Sensing*, vol. 61, pp. 1–13, 2023.
- [21] S. Chen, L. Ji, S. Zhu, M. Ye, H. Ren, and Y. Sang, "Toward dense moving infrared small target detection: New datasets and baseline," *IEEE Transactions on Geoscience and Remote Sensing*, vol. 62, pp. 1–13, 2024.
- [22] Y. Gao, Y. Feng, S. Ji, and R. Ji, "Hgnn+: General hypergraph neural networks," *IEEE Transactions on Pattern Analysis and Machine Intelligence*, vol. 45, no. 3, pp. 3181–3199, Mar. 2023.
- [23] Y. Feng, J. Huang, S. Du, S. Ying, J.-H. Yong, Y. Li, G. Ding, R. Ji, and Y. Gao, "Hyper-yolo: When visual object detection meets hypergraph computation," *IEEE Transactions on Pattern Analysis and Machine Intelligence*, pp. 1–14, 2025.
- [24] Y. Gao, Z. Zhang, H. Lin, X. Zhao, S. Du, and C. Zou, "Hypergraph learning: Methods and practices," *IEEE Transactions on Pattern Analysis and Machine Intelligence*, vol. 44, no. 5, pp. 2548–2566, 2022.
- [25] D. Yang, B. Qu, J. Yang, and P. Cudré-Mauroux, "Lbsn2vec++: Heterogeneous hypergraph embedding for location-based social networks," *IEEE Transactions on Knowledge and Data Engineering*, vol. 34, no. 4, pp. 1843–1855, 2022.
- [26] R. Viñas, C. K. Joshi, D. Georgiev, P. Lin, B. Dumitrascu, E. R. Gamazon, and P. Liò, "Hypergraph factorization for multi-tissue gene expression imputation," *Nature Machine Intelligence*, vol. 5, no. 7, pp. 739–753, Jul. 2023.
- [27] L. Xiao, J. Wang, P. H. Kassani, Y. Zhang, Y. Bai, J. M. Stephen, T. W. Wilson, V. D. Calhoun, and Y.-P. Wang, "Multi-hypergraph learning-based brain functional connectivity analysis in fmri data," *IEEE Transactions on Medical Imaging*, vol. 39, no. 5, pp. 1746–1758, May 2020.
- [28] S. D. Deshpande, M. H. Er, R. Venkateswarlu, and P. Chan, "Max-mean and max-median filters for detection of small targets," in *SPIE's International Symposium on Optical Science, Engineering, and Instrumentation*, Denver, CO, Oct. 1999, pp. 74–83.
- [29] J. Han, K. Liang, B. Zhou, X. Zhu, J. Zhao, and L. Zhao, "Infrared small target detection utilizing the multiscale relative local contrast measure," *IEEE Geoscience and Remote Sensing Letters*, vol. 15, no. 4, pp. 612–616, Apr. 2018.
- [30] J. Han, S. Moradi, I. Faramarzi, H. Zhang, Q. Zhao, X. Zhang, and N. Li, "Infrared small target detection based on the weighted strengthened local contrast measure," *IEEE Geoscience and Remote Sensing Letters*, vol. 18, no. 9, pp. 1670–1674, Sep. 2021.
- [31] J. Han, S. Moradi, I. Faramarzi, C. Liu, H. Zhang, and Q. Zhao, "A local contrast method for infrared small-target detection utilizing a tri-layer window," *IEEE Geoscience and Remote Sensing Letters*, vol. 17, no. 10, pp. 1822–1826, Oct. 2020.
- [32] O. Ronneberger, P. Fischer, and T. Brox, "U-net: Convolutional networks for biomedical image segmentation," in *Medical Image Computing and Computer-Assisted Intervention – MICCAI 2015*, Cham, 2015, pp. 234–241.
- [33] M. Zhang, R. Zhang, Y. Yang, H. Bai, J. Zhang, and J. Guo, "Isnet: Shape matters for infrared small target detection," in *2022 IEEE/CVF Conference on Computer Vision and Pattern Recognition (CVPR)*, Jun. 2022, pp. 867–876.
- [34] H. Sun, J. Bai, F. Yang, and X. Bai, "Receptive-field and direction induced attention network for infrared dim small target detection with a large-scale dataset irdst," *IEEE Transactions on Geoscience and Remote Sensing*, vol. 61, pp. 1–13, 2023.
- [35] M. Zhang, H. Bai, J. Zhang, R. Zhang, C. Wang, J. Guo, and X. Gao, "Rkformer: Runge-kutta transformer with random-connection attention for infrared small target detection," in *Proceedings of the 30th ACM International Conference on Multimedia*, New York, NY, USA, Oct. 2022, pp. 1730–1738.
- [36] T. Chen, Q. Chu, Z. Tan, B. Liu, and N. Yu, "Abmnet: Coupling transformer with cnn based on adams-bashforth-moulton method for infrared small target detection," in *2023 IEEE International Conference on Multimedia and Expo (ICME)*, Brisbane, Australia, Jul. 2023, pp. 1901–1906.
- [37] B. Li, Y. Wang, L. Wang, F. Zhang, T. Liu, Z. Lin, W. An, and Y. Guo, "Monte carlo linear clustering with single-point supervision is enough for infrared small target detection," in *2023 IEEE/CVF International Conference on Computer Vision (ICCV)*, Oct. 2023, pp. 1009–1019.
- [38] X. Ying, L. Liu, Y. Wang, R. Li, N. Chen, Z. Lin, W. Sheng, and S. Zhou, "Mapping degeneration meets label evolution: Learning infrared small target detection with single point supervision," in *2023 IEEE/CVF Conference on Computer Vision and Pattern Recognition (CVPR)*, Vancouver, BC, Canada, Jun. 2023, pp. 15 528–15 538.
- [39] D. Yang, H. Zhang, Y. Li, and Z. Jiang, "Label evolution based on local contrast measure for single-point supervised infrared small-target detection," *IEEE Transactions on Geoscience and Remote Sensing*, vol. 62, pp. 1–12, 2024.
- [40] H. Li, J. Yang, Y. Xu, and R. Wang, "A level set annotation framework with single-point supervision for infrared small target detection," *IEEE Signal Processing Letters*, vol. 31, pp. 451–455, 2024.
- [41] R. Kou, C. Wang, Q. Fu, Z. Li, Y. Luo, B. Li, W. Li, and Z. Peng, "Mcgc: A multiscale chain growth clustering algorithm for generating infrared small target mask under single-point supervision," *IEEE Transactions on Geoscience and Remote Sensing*, vol. 62, pp. 1–12, 2024.
- [42] R. Ni, J. Wu, Z. Qiu, L. Chen, C. Luo, F. Huang, Q. Liu, B. Wang, Y. Li, and Y. Li, "Point-to-point regression: Accurate infrared small target detection with single-point annotation," *IEEE Transactions on Geoscience and Remote Sensing*, vol. 63, pp. 1–19, 2025.
- [43] Y. Lu, Y. Lin, H. Wu, X. Xian, Y. Shi, and L. Lin, "Sirst-5k: Exploring massive negatives synthesis with self-supervised learning for robust infrared small target detection," *IEEE Transactions on Geoscience and Remote Sensing*, vol. 62, pp. 1–11, 2024.
- [44] T. Chen, Z. Ye, Z. Tan, T. Gong, Y. Wu, Q. Chu, B. Liu, N. Yu, and J. Ye, "Mim-istd: Mamba-in-mamba for efficient infrared small-target detection," *IEEE Transactions on Geoscience and Remote Sensing*, vol. 62, pp. 1–13, 2024.
- [45] M. Zhang, Y. Wang, J. Guo, Y. Li, X. Gao, and J. Zhang, "Irsam: Advancing segment anything model for infrared small target detection," in *ECCV 2024*, Cham, 2025, vol. 15125, pp. 233–249.
- [46] P. Yan, R. Hou, X. Duan, C. Yue, X. Wang, and X. Cao, "Stdmanet: Spatio-temporal differential multiscale attention network for small moving infrared target detection," *IEEE Transactions on Geoscience and Remote Sensing*, vol. 61, pp. 1–16, 2023.
- [47] R. Li, W. An, C. Xiao, B. Li, Y. Wang, M. Li, and Y. Guo, "Direction-coded temporal u-shape module for multiframe infrared small target detection," *IEEE Transactions on Neural Networks and Learning Systems*, pp. 1–14, 2025.
- [48] S. Zhu, L. Ji, J. Zhu, S. Chen, and W. Duan, "Tmp: Temporal motion perception with spatial auxiliary enhancement for moving infrared dim-small target detection," *Expert Systems with Applications*, vol. 255, p. 124731, Dec. 2024.
- [49] W. Duan, L. Ji, S. Chen, S. Zhu, and M. Ye, "Triple-domain feature learning with frequency-aware memory enhancement for moving infrared small target detection," *IEEE Transactions on Geoscience and Remote Sensing*, vol. 62, pp. 1–14, 2024.
- [50] W. Duan, L. Ji, J. Huang, S. Chen, S. Peng, S. Zhu, and M. Ye, "Semi-supervised multiview prototype learning with motion reconstruction for moving infrared small target detection," *IEEE Transactions on Geoscience and Remote Sensing*, vol. 63, pp. 1–15, 2025.
- [51] S. Chen, L. Ji, W. Duan, S. Peng, and M. Ye, "Motion prior knowledge learning with homogeneous language descriptions for moving infrared small target detection," *Proceedings of the AAI Conference on Artificial Intelligence*, vol. 39, no. 2, pp. 2186–2194, Apr. 2025.
- [52] Z. Ge, S. Liu, F. Wang, Z. Li, and J. Sun, "Yolox: Exceeding yolo series in 2021," Aug. 2021.
- [53] Y. Wang, H. Wu, J. Zhang, Z. Gao, J. Wang, P. S. Yu, and M. Long, "Predrnn: A recurrent neural network for spatiotemporal predictive learning," *IEEE Transactions on Pattern Analysis and Machine Intelligence*, vol. 45, no. 2, pp. 2208–2225, Feb. 2023.
- [54] S. Tang, C. Li, P. Zhang, and R. Tang, "Swinlstm: Improving spatiotemporal prediction accuracy using swin transformer and lstm," in *Proceedings of the IEEE/CVF International Conference on Computer Vision*, 2023, pp. 13 470–13 479.
- [55] Y. Dai, Y. Wu, F. Zhou, and K. Barnard, "Attentional local contrast networks for infrared small target detection," *IEEE Transactions on Geoscience and Remote Sensing*, vol. 59, no. 11, pp. 9813–9824, Nov. 2021.
- [56] T. Wu, B. Li, Y. Luo, Y. Wang, C. Xiao, T. Liu, J. Yang, W. An, and Y. Guo, "Mtu-net: Multilevel transunet for space-based infrared tiny ship detection," *IEEE Transactions on Geoscience and Remote Sensing*, vol. 61, pp. 1–15, 2023.
- [57] Q. Liu, R. Liu, B. Zheng, H. Wang, and Y. FU, "Infrared small target detection with scale and location sensitivity," in *2024 IEEE/CVF Conference on Computer Vision and Pattern Recognition (CVPR)*, 2024, pp. 17 490–17 499.

- [58] F. Wu, T. Zhang, L. Li, Y. Huang, and Z. Peng, "Rpcanet: Deep unfolding rpca based infrared small target detection," in *2024 IEEE/CVF Winter Conference on Applications of Computer Vision (WACV)*, 2024, pp. 4797–4806.
- [59] Y. Dai, P. Pan, Y. Qian, Y. Li, X. Li, J. Yang, and H. Wang, "Pick of the bunch: Detecting infrared small targets beyond hit-miss trade-offs via selective rank-aware attention," *IEEE Transactions on Geoscience and Remote Sensing*, vol. 62, pp. 1–15, 2024.
- [60] B. Hui, Z. Song, H. Fan, P. Zhong, W. Hu, X. Zhang, J. Lin, H. Su, W. Jin, Y. Zhang, and Y. Bai, "A dataset for infrared image dim-small aircraft target detection and tracking under ground / air background," Oct. 2019.